CHEMICAL ENGINEERING TRANSACTIONS
VOL. 74, 2019
A publication of AIDIC
The Italian Association of Chemical Engineering
Online at www.cetjournal.it
Guest Editors: Sauro Pierucci, Jiří Jaromír Klemeš, Laura Piazza

ISBN 978-88-95608-71-6; **ISSN** 2283-9216
DOI: 10.3303/CET1974179

Predicting Intrinsic Permeability of a Double Porosity Cellular Ceramic using X-Ray Micro-Tomography

Iara F. Mantovani[a,*], Leandro Coser[a], Clara M. B. Calado[b], Odair J. Bellini[a], Dachamir Hotza[a,b], Mara G. N. Quadri[b], Celso P. Fernandes[a]

[a]Graduate Program in Materials Science and Engineering – PGMAT, Laboratory of Porous Media and Thermophysical Properties – LMPT, Federal University of Santa Catarina - UFSC, 88040 900 Florianópolis - SC, Brazil
[b]Department of Chemical Engineering and Food Engineering, Federal University of Santa Catarina - UFSC, 88040 900 Florianópolis - SC, Brazil
iara@lmpt.ufsc.br

The microstructure of a porous cellular ceramic exhibiting two spatial characteristic lengths was characterized to determine parameters of its pore space morphology and connectivity. In order to assess the hierarchical microstructure, X-ray computed micro-tomography was employed as an imaging technique to supply three-dimensional images in two spatial scales. Two samples, at different sintering temperatures, were produced by emulsification of sunflower oil in aqueous aluminum oxide suspensions using gelatin bloom 90 as the gelling agent, dodecyl sodium sulfate as the surfactant and native cassava starch as the gelling and porogenic agent. Image processing and morphological characterization were performed on each spatial scale, individually allowing the calculation of the total porosity and pore size distribution of the ceramic sample. For the numerical simulation of the intrinsic permeability, representative images of the two spatial scales were superposed in a single super-image. This simulation was performed on the 3D pore network extracted from the super-image. The simulated permeability results were interpreted on the basis of the microstructure.

1. Introduction

The main purpose in materials science and engineering is to develop materials with macroscopic properties adequate to a specific application. Materials macroproperties are highly influenced by their microstructure, including intrinsic properties of the phases such as their quantity, morphology and connectivity.

A wide variety of porous ceramics are used for various applications including filtration, adsorption and catalysis, tissue engineering, and fuel cells (Gerke et al., 2015). Important physical properties of these ceramics, such as permeability, thermal and electric conductivity and mechanical resistance are closely related to their microstructure. For instance, intrinsic permeability depends on the effective (open) porosity, pore size distribution and the connectivity of the pore space.

The quantitative description of the morphology and connectivity of porous ceramics becomes important for a better understanding of the relationship between properties and microstructure. For this purpose, 3D images obtained by means of X-ray computed micro-tomography (μCT) coupled with image analysis are currently very common (Appoloni et al., 2004; Maire et al., 2007; Gerke et al., 2015; Gregorová et al., 2018; Lux et al., 2018).

Besides morphological characterization, 3D images make it possible to assess macroscopic properties by numerical simulation of physical phenomena in representative elementary volumes of the material. In addition, numerical simulation of properties is important because sometimes laboratory measurement can require a complex or time-consuming procedure, and can even cause sample brittleness (Gerke et al., 2015).

As well as porous ceramics, a wide class of materials can exhibit several spatial length scales such as carbonate rocks and cementitious materials. The microstructure of these multiscale materials is composed of multiple porosities organized hierarchically. The description and numerical simulation of properties of such a hierarchical microstructure is a challenge and can involve the combination of complementary

Paper Received: 10 July 2018; Revised: 21 November 2018; Accepted: 19 February 2019

Please cite this article as: Mantovani I., Coser L., Calado C., Bellini O.J., Dachamir H., Quadri M., Fernandes C., 2019, Predicting Intrinsic Permeability of a Double Porosity Cellular Ceramic Using X-ray Micro-tomography, Chemical Engineering Transactions, 74, 1069-1074 DOI:10.3303/CET1974179

techniques as shown in the work of Gregorová et al. (2018) using mercury porosimetry, stereology techniques on 2D images, and 3D images acquired with X-ray micro-tomography.
In this article, we present a workflow of image processing and analysis that characterizes the morphology and simulates the intrinsic permeability of a double porosity ceramic from 3D images of two spatial scales obtained using X-ray micro-tomography.
Among the various methods to numerically simulate the intrinsic or Darcy permeability, the approach based on the pore network extracted from the 3D porous space of µCT images was used (Dong and Blunt, 2009). Besides permeability, the pore network representation was also used for the determination of the coordination number and average throat size.

2. Materials and Methods

2.1 Porous ceramic preparation via gelcasting

The development of the ceramic samples was accomplished by emulsification of sunflower oil in aqueous aluminum oxide (alumina, Al_2O_3) suspensions using gelatin bloom 90 as the gelling agent, dodecyl sodium sulfate as the surfactant and native cassava starch as the gelling and porogenic agent, as described elsewhere (Calado, 2017). In a muffle oven, the organic compounds were removed at a heating rate of 2° C/min up to 1100° C, followed by a 2 h isothermal plateau. Sintering was carried out in a tubular furnace at a heating rate of 2° C/min to 1400° C or 1550° C with a final 2-h plateau to produce the samples under study: S11 and E11.

2.2 Porous ceramic characterization via 3D image processing

Image acquisition
An X-ray computed micro-tomograph (Zeiss Versa XRM-500) was used to observe and characterize the details of the internal structure of the samples at a spatial resolution of micrometer-order. Typically, the sample preparation is minimal, and the technique is mostly nondestructive, allowing many scans to be made at the same sample under different conditions. However, there is a trade-off between spatial resolution and sample size: high resolutions require small samples. Because of this, one single tomography acquisition image is often unable to show the entire pore size distribution of the sample. To address this problem, an original volume and a sub-volume of the ceramics were scanned under appropriate spatial resolutions, allowing each of them to show a certain range of pore sizes. Figures 1a and 1c show sample images, represent with low-resolution (LR), which is a plug of 6 mm x 10 mm (diameter and height). The high-resolution (HR) images required a sub-volume cut from the plugs (Figures 1b and 1d) with 1 mm x 3 mm of dimension. The voxel sizes of the LR and HR images are 6.8 µm and 1.2 µm, respectively.

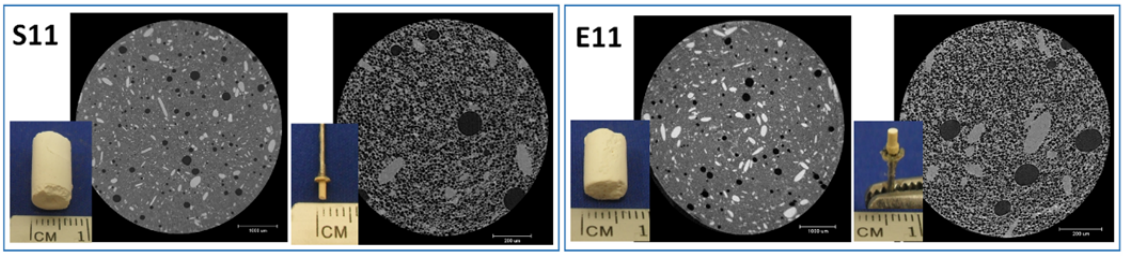

Figure 1. µCT images of S11 and E11. Figures (a) and (c) LH images (6.8 µm) acquired from samples of 6 mm x 10 mm. Figures (b) and (d) HR images (1.2 µm) acquired from sub-volume of 1 mm x 3 mm.

Image processing
An anisotropic diffusion filter was applied to the original low resolution µCT images (Figure 1a and 1c) after the VOI (volume of interest) delimitation (Weickert, 2001). This filtering operation was used to minimize internal variability in regions whilst preserving the contour between regions. Then, a classification was performed using Polynomial Mahalanobis (Grudic and Mulligan, 2006) to determine data grouping, denominated as pore, solid (alumina agglomerates) and non-solved (grey regions in Figure 1a and c). Applying a threshold to these regions, definitive phases inside the images of scale 1 were determined. Original high-resolution images (Figure 1b and 1d) were directly submitted for classification without filtering, resulting in two groups of data. Again, after classification, a threshold was applied confirming these regions and classifying every voxel as pore or solid. Image processing, morphological characterization and permeability simulation were performed dedicated software (Imago3D, LMPT/UFSC).

Image characterization

Once the pore space was segmented, the pore size distribution was measured in both LR and HR images, by opening morphological operation, i.e., erosion followed by dilation (Coster and Chermant, 1989). The opening operation was applied to the so-called background distance image using the chamfer metric $d_{3\text{-}4\text{-}5}$ to generate the 3D balls (Borgefors, 1986; Thiel and Montanvert, 1992).

The 3D pore space can be represented in a pore network model where the pore space is partitioned in two basic elements: large voids (called pores) and constrictions throats that connect, at least, two pores. In general, spheres and cylinders are used to represent pores and constrictions, respectively. The computational code was constructed based on the maximal ball method (Silin and Patzek, 2006; Dong and Blunt, 2009). The original volume of pores and throats as well as the connectivity of the pore space is preserved in the pore network model. In the present work, the pore network representation for the numerical calculation of the Darcian permeability was used.

Porosity and pore size distribution were calculated in each spatial scale (individually) and afterwards placed together using a multiscale composition model developed for additive properties (Papadopoulos et al., 2009; Mantovani, 2013). The mathematical model is based on the fact that the LR image (scale 1 – s1) is composed of two well-defined regions of porosity and solids, and a third region, where it is difficult to ascertain if it is either composed of solids or by sub-micro pores under the spatial resolution. The undefined elements of this region, named as non-solved region, can be solved in the HR image (scale 2 – s2). The total porosity ϕ_T of the sample quantified considering the two spatial scales (images LR and HR), is given by:

$$\phi_T = \phi_1 + I_1\phi_2 \tag{1}$$

where I_1 is the volume fraction of non-solved region in scale 1, and ϕ_1 and ϕ_2 are the porosities of scale 1 and 2, respectively. Considering $f_i(r)$ as the pore size distribution, i.e., the volumetric fractions measured for each *i* (*i* = 1, 2) scale, the total pore size distributions $f_1^T(r)$ and $f_2^T(r)$ can be given, respectively, by:

$$f_1^T(r) = f_1(r)\frac{\phi_1}{\phi_T} \quad \text{and} \quad f_2^T(r) = f_2(r)\frac{\phi_2 I_1}{\phi_T} \tag{2}$$

In these equations, each scale covers a range of radii of pores (r) and there is no intersection between each range.

The REV (Representative Elementary Volume) concept defines the minimum volume in a pore system for which the continuum assumption is valid; so, in this volume, macroscopic properties can be calculated. In this work, we determined the REV for porosity testing random subvolumes extracted from the super-image. The subvolumes sizes (V_L) were increased in edge length (L) until the porosity converged to a certain tolerance, (±δ). With this procedure, the minimum edge length L_{VER} that defines REV is (Petrasch et al., 2008):

$$L_{VER} = min\{L \leq L^* | \, \phi - \delta < \phi(V_{L^*}) < \phi + \delta\}, \quad \delta \ll 1 \tag{3}$$

2.3 Super-image Permeability Numerical Simulation

Using the pore network model, it was possible to simulate the Darcian permeability of scales 1 (LR image) and 2 (HR image) individually. There are models proposed to simulate permeability of multiscale systems from the pore network extracted from each scale, such as the model of Jiang et al (2013). In this case, for the particular dual porosity microstructure analyzed, permeability was predicted using the pore network extracted directly from a so-called super-image, obtained by the combination of LR and HR images as follows. The procedure starts by cropping a representative region of scale 1 (LR image) and scale 2 (HR image). First, let´s consider R the ratio between the voxel size of LR and HR images. For the images analyzed here, R is approximated by six. Then, the size of the selected cropped section of the LR image is enlarged so that each voxel has the same size of the HR image. To do this, each voxel of the LR image is replicated R times on the three orthogonal directions of the image. The cropped section of the LR image is composed of three regions: pore space, solids and non-solved region. Voxels of the last region are shown by the HR image. These voxels are replaced by inserting the cropped section of the HR image into the regions of non-solved voxels of the enlarged LR image, keeping untouched voxels which were already labeled as pore or solid. In this operation, the cropped section of the HR image is repeatedly rotated and reinserted into the super-image until it completely fills the non-solved region. At the end of this procedure, the super-image is obtained, which is composed solely of voxels labeled as pore and solid, statistically representing the entire microstructure of the ceramics (scale 1 with scale 2). The linear size of the super-

image will be the size of the sample of LR image multiplied by R. In the super-image, the pore network is extracted, and the permeability is simulated.

3. Results and discussion

Examples of 3D images, before and after the segmentation process, are shown in Figure 2 for the sample S11 in both spatial scales (LR and HR images). We can observe the spherical shape of pores and the agglomerates of alumina particles in scale 1. The volume fraction and geometrical configuration of phases presented by sample E11 display similar behavior to those of sample S11.

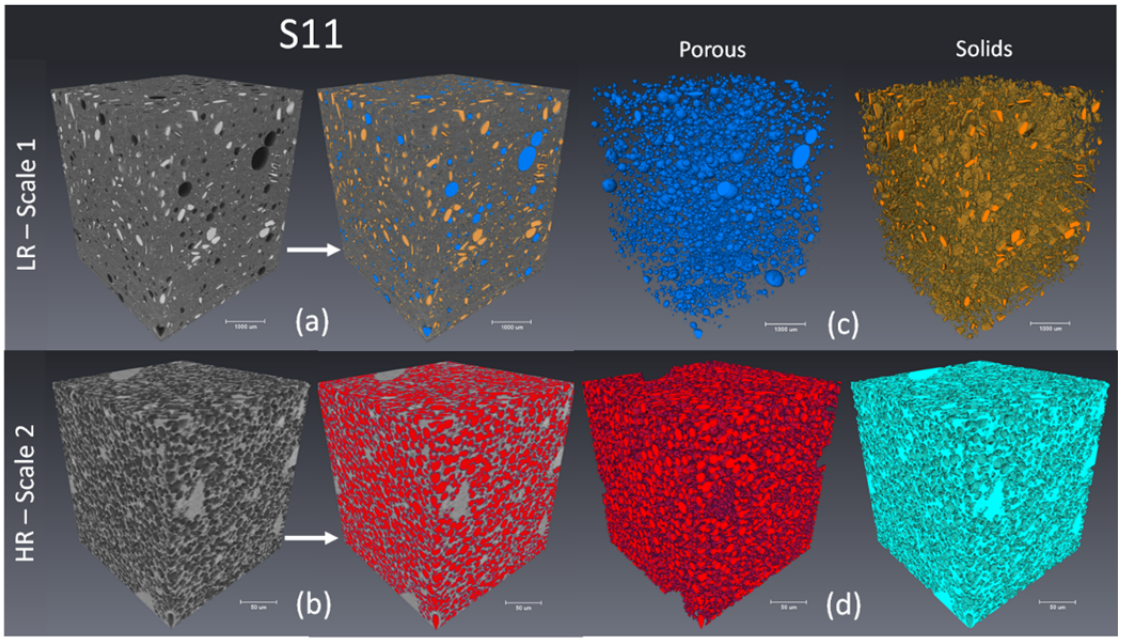

Figure 2. Segmentation image processing of sample S11. (a) LR images segmented in three-phases: porous (blue), solid (orange) and non-solved region (gray). (b) HR images segmented in porous (red) and solid (light green). (c) and (d) individual pores and solid phases from the whole sample. Scale length to LR images is 1000 µm and to HR images is 50 µm.

Image processing results in the phase segmentation of samples S11 and E11 as porous, solid and non-solved regions for scale 1, and pore and solid for scale 2 quantifying their volume fractions. The data obtained from the images in each scale was the input data for the multiscale model (Eq(1) and Eq(2)), quantifying the cellular ceramics as a whole. Table 1 shows volume fraction values as well as the average coordination number and Darcian permeability calculated by pore network modeling.

Table 1: Phase fraction (pores and solids), in each scale, and in entire sample determined by multiscale model and in the super-image.

Sample	Scale/ Resolution (µm)	Solid fraction (%)	Pore fraction (%)	Average coordination number	Darcian permeability (mD)
S11	s1/6.82	8.61	3.87	-	0.00
	s2/1.17	61.61	38.39	3.90	43.90
	Multiscale	62.53	37.47	-	-
	Super-Image	67.77	35.23	4.00	25.10
E11	s1/6.82	7.11	3.35	-	0.00
	s2/1.17	55.90	44.10	4.30	43.50
	Multiscale	57.17	42.84	-	-
	Super-Image	57.97	42.03	4.40	32.80

Figure 3 shows the REV of samples S11 and E11 determined by porosity in relation to sub-volumes taken at random positions inside the VOI used in the image processing. These sub-volumes were then enlarged in increments of 10^3 voxels (20^3, 30^3, 40^3…) until the entire volume of the super-image was reached.
The pore size distributions measured using opening for each spatial scale for samples S11 and E11 are shown in Figure 4a. Figure 4b presents the total pore distribution measured (by opening) in the super-image compared to that calculated by multiscale Eq(2) with the data presented in Figure 4a.

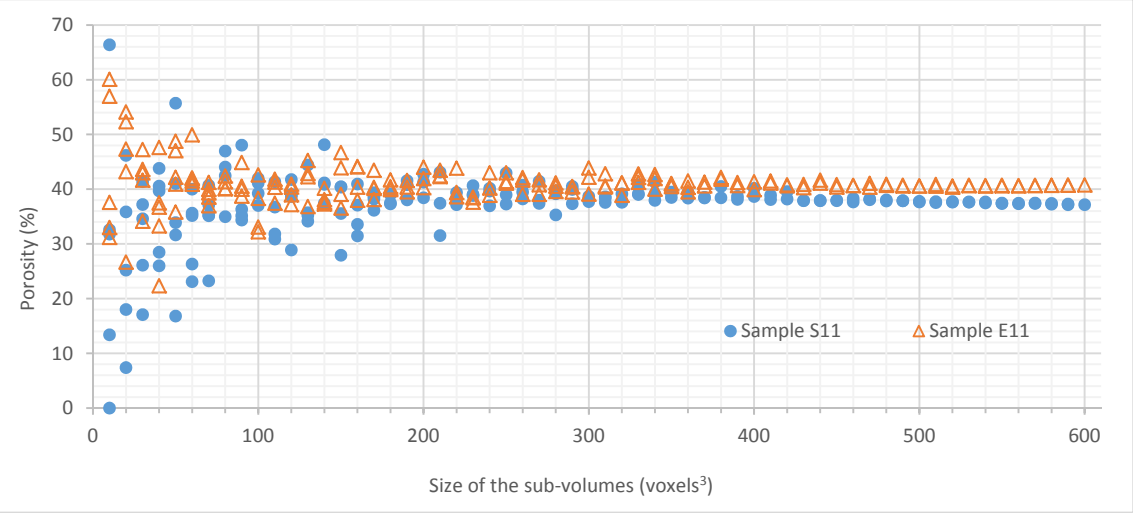

Figure 3. Representative Elementary Volume for the porosity of the samples S11 and E11 determined in the super-image.

The 3D image characterization allows comparison of the morphology and the connectivity of the porous spaces of the ceramics samples E11 and S11. The pore size distribution (Figure 4) showed similarity between E11 and S11 essentially when the spatial scale 2 (HR image) was considered. Using the pore network modeling, we calculated the average throat size of scale 2 as approximately 0.9 µm and 0.8 µm for S11 and E11, respectively. Considering the super-image, it can be observed from Table 1 that the sample E11 has porosity and an average coordination number larger than the S11 sample. From super-images, the values of the simulated Darcian permeability of approximately 25 mD were obtained for S11 and ~35 mD for E11, probably due to the slightly better connectivity and larger porosity in the latter case. Individually, scale 1 from both E11 and S11 correspond to non-percolating systems; the percolation arises due the connectivity between the pores of scale 2. Therefore, the hydraulic resistance of the fluid flow in samples S11 and E11 are governed by scale 2. The results obtained for the total porosity and total pore size distribution were very close considering the calculation by the multiscale model and the measurement on the super-image.

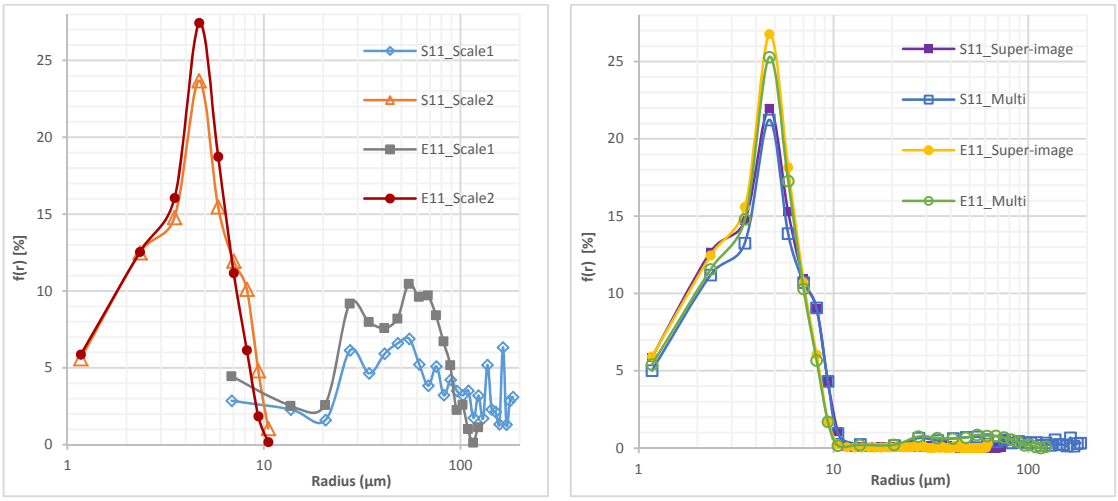

(a) (b)

Figure 4. Pore size distribution for (a) each scale, and (b) composed as total (bimodal) by multiscale model and measured in the super-image. All distributions determined by mathematical morphology.

4. Conclusions

A morphological characterization of ceramics samples with dual porosity on 3D μCT images was carried out in this paper using a proposed image analysis pipeline. Total porosity and total pore size distribution were determined either by a multiscale model or by a constructed super-image that encompass microstructural features of both spatial scales. Results from the super-image and multiscale model are in good agreement. The permeability of the two samples was interpreted based on the morphology and connectivity of the microstructures. The analysis based on 3D images, particularly in the case of porous materials with two or more characteristic length scales, is a powerful tool for a better understanding of the relationship between microstructure and macroscopic properties.

Acknowledgments

The authors thank the Conselho Nacional de Desenvolvimento Científico e Tecnológico (CNPq), Coordenação de Aperfeiçoamento de Pessoal de Nível Superior (CAPES) and PETROBRAS.

References

Appoloni C.R., Fernandes C.P., Innocentini M.D.M, Macedo A., 2004, Ceramic foams porous microstructure characterization by X-ray microtomography, Materials Research, 7(4), 557-564.

Borgefors G., 1986, Distance transformations in digital images, Computer Vision, Graphics, and Image Processing, 34, 344-371.

Calado C.M.B., 2017, Cerâmicas celulares obtidas a partir da emulsificação de suspensões de alumina com óleo de girassol, amido e gelatina, Master thesis, Federal University of Santa Catarina (in Portuguese).

Coster M., and Chermant J.L., 1989, Precis d'analyse d'images, Presses du CNRS, Paris (in French).

Dong H. and Blunt M., 2009, Pore-network extraction from micro-computerized-tomography images, Physical Review E, 80(3), 1-11.

Gerke K.M., Korost D.V., Vasilyev R.V., Karsanina M.V., Tarasovskii, V.P., 2015, Studying structure and determining permeability of materials based on X-Ray microtomography data (using porous ceramics as an example), Inorganic Materials 51(9), 951-957.

Gregorová E., Uhlířová T., Pabst W., Diblíková P., Sedlářová I., 2018, Microstructure characterization of mullite foam by image analysis, mercury porosimetry and X-ray computed microtomography, Ceramics International, 44(11), 12315-12328.

Grudic G., Mulligan J., 2006, Outdoor path labeling using polynomial mahalanobis distance, Robotics: Science and Systems II Conference, University of Pennsylvania, Philadelphia, Pennsylvania, USA.

Jiang Z., van Dijke M.I.J., Sorbie K.S., Couples G.D., 2013, Representation of multi-scale heterogeneity via multi-scale pore networks, Water Resources Research, 49, 5437–5449.

Lux J., Guzi de Moraes E., Maire E., Adrien J., Biasett, L., 2018, Gas permeability of Ti6Al4V foams prepared via gelcasting, experiments and modelling, Computational Materials Science, 152, 363-373.

Maire E., Colombo P., Adrien J., Babout L., Biasetto l., 2007, Characterization of the morphology of cellular ceramics by 3D image processing of X-ray tomography, Journal of the European Ceramic Society, 27(4), 1973-1981.

Mantovani I.F., 2013, Microtomografia e nanotomografia de raios X aplicada à caracterização multiescalar de sistemas porosos carbonáticos. PhD thesis, Federal University of Santa Catarina (in Portuguese).

Papadopoulos, A., Whitmore A.P., White R.P., Mooney S. J., and Bird N.R.A., 2009, Combining Spatial Resolutions in the Multiscale Analysis of Soil Pore-Size Distributions, Vadose Zone Journal, 8(1), 227.

Petrasch J., Wyss P., Stämpfli R., Steinfeld A., 2008, Tomography-Based Multiscale Analyses of the 3D Geometrical Morphology of Reticulated Porous Ceramics, The American Ceramic Society, 9(8), 2659-2665.

Silin D., Patzek T., 2006, Pore space morphology analysis using maximal inscribed spheres, Physica A: Statistical Mechanics and its Applications, 371(2), 330–360.

Thiel E. and Montanvert A., 1992, Shape splitting from medial lines using the 3–4 chamfer distance, Proceedings., 11th IAPR International Conference on Pattern Recognition. Vol. III. Conference C: Image, Speech and Signal Analysis, New York: Plenum, 537–546.

Weickert J., 2001, Applications of nonlinear diffusion in image processing and computer vision, Acta Mathematica Universitatis Comenianae, 70(1), 33-50.